Effect of topology on quasiparticle interactions in the Weyl semimetal WP$_2$

Dirk Wulferding [1,2,*] Peter Lemmens [1,2] Florian Büscher,[1,2] David Schmeltzer [3]
Claudia Felser,[4] and Chandra Shekhar [4]

[1]*Institute for Condensed Matter Physics, TU Braunschweig, Mendelssohnstrasse 3, 38106 Braunschweig, Germany*
[2]*Laboratory for Emerging Nanometrology, TU Braunschweig, Langer Kamp 6, 38106 Braunschweig, Germany*
[3]*Physics Department, City College of the City University of New York, New York 10031, USA*
[4]*Max Planck Institute for Chemical Physics of Solids, Nöthnitzer Strasse 40, 01187 Dresden, Germany*

We compare two crystallographic phases of the low-dimensional WP$_2$ to better understand features of electron-electron and electron-phonon interactions in topological systems. The topological β phase, a Weyl semimetal with a giant magnetoresistance, shows a larger intensity of electronic Raman scattering compared to the topologically trivial α phase. This intensity collapses for $T < T^* = 20$ K, which evidences a crossover in the topological phase from marginal quasiparticles to a coherent low-temperature regime. In contrast, the topologically trivial α phase shows more pronounced signatures of electron-phonon interaction, i.e., an enhanced phonon linewidth and deviations from conventional anharmonicity in an intermediate-temperature regime. These effects provide evidence for an interesting interplay of electronic correlations and electron-phonon coupling. Interband and intraband electronic fluctuations can be distinguish by the energy range of electronic Raman scattering and their temperature dependence. Furthermore, we demonstrate a decisive dependency on symmetry that is critical to understand their interplay.

I. INTRODUCTION

Recently, the aspect of topology in condensed-matter physics has gained immense importance, leading to the experimental discovery of novel phases—topological insulators, Dirac semimetals, and Weyl semimetals—in systems with strong spin-orbit coupling [1,2]. These emergent topological phases are governed by Chern numbers and symmetry aspects of the electronic band structure close to the Fermi energy. Weyl semimetals with low energy, chiral fermions require the breaking of at least time-reversal or inversion symmetry. Otherwise, they can be classified either as Dirac semimetals or as topologically trivial materials.

While so far the focus has been mainly on single-particle physics, the importance of interactions, such as electronic correlations and electron-phonon interaction, has been emphasized recently. The former are relevant, e.g., in certain pyrochlores [3], while the latter could be relevant if there is a matching of typical phonon and electronic energy scales. Electron-phonon interactions can be used to characterize the electronic band topology or even induce a topological phase [4–7]. Related phonon anomalies have, indeed, been observed in Raman scattering (RS) of the Dirac semimetal Cd$_3$As$_2$ [8] and the Weyl semimetal NbIrTe$_4$ [9].

Here, we present a comparative Raman spectroscopic study of two structural modifications of WP$_2$, the topologically trivial α phase and the topologically relevant β phase. The latter is a robust type-II Weyl semimetal, which means that

Weyl points with tilted three-dimensional cones exist at the intersection of hole and electron pockets. A prerequisite for the existence of such Weyl points is broken inversion symmetry [10]. Furthermore, neighboring Weyl points in β-WP$_2$ have the same chirality, which enhances their stability and robustness against lattice distortions. Indeed, no appreciable temperature dependence of the electronic band structure and topological features has been observed in the temperature range 25–170 K [11].

The β phase evidences strong electron-electron correlations with a hydrodynamic regime of charge transport for $T < T^* = 20$ K [12]. In this regime resistivity depends on sample dimensions and is nondiffusive. Transport is also highly anisotropic and enhanced along the chainlike arrangement of tungsten-phosphorus polyhedra. There exist a giant magnetoresistance of 4×10^6%, a residual low-temperature resistivity of 3 nΩ cm, and a charge carrier mean free path of 0.5 mm [13]. Band structure calculations of the monoclinic α phase point to a trivial electronic band structure with a center of inversion. Nevertheless, it shows an appreciable magnetoresistance of 5×10^5% and a residual low-temperature resistivity of 42 nΩ cm [14]. These dissimilar properties call for a detailed comparison of the relevant scattering mechanisms and correlation effects in the two phases.

Our study shows quasielastic and finite-energy electronic Raman scattering (ERS) in both phases, which is a fingerprint of electronic correlations and/or nesting. In the topological β phase the finite-energy scattering shows a sharp drop in intensity for temperatures below approximately 50 K that initiates the electronic crossover to hydrodynamic charge transport at $T^* = 20$ K. The topological phase also shows a larger intensity of quasielastic scattering with a more

*Present address: Center for Correlated Electron Systems, Institute for Basic Science, Seoul 08826, Republic of Korea.
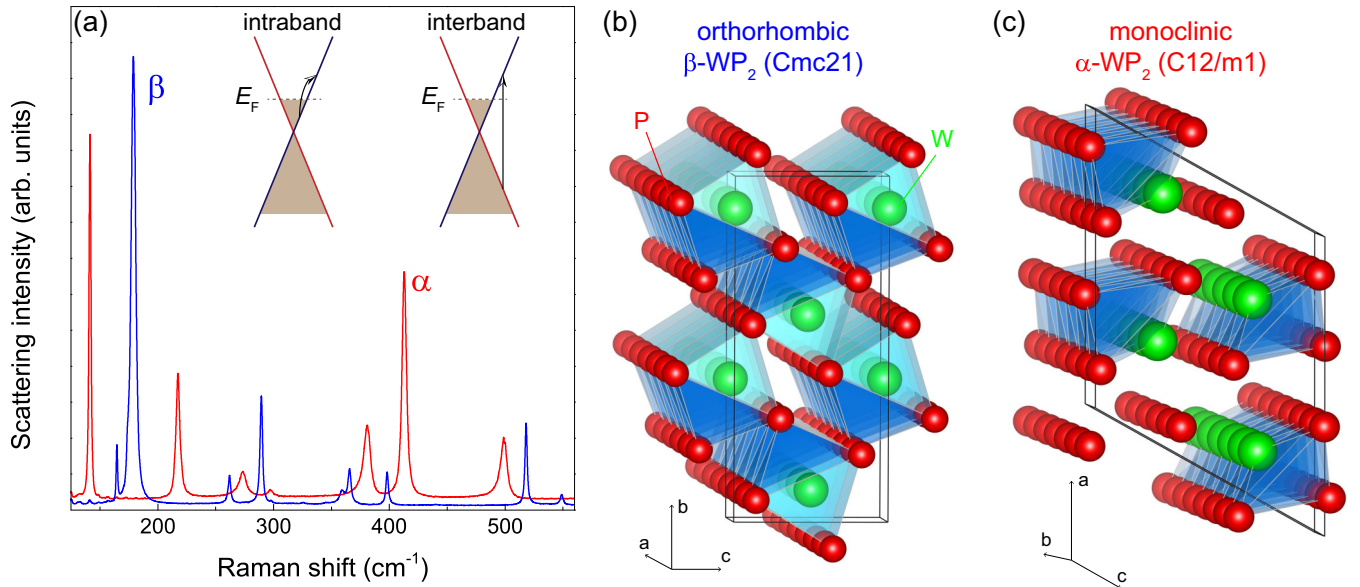
FIG. 1. (a) Unpolarized room-temperature Raman spectra of the orthorhombic β-WP$_2$ (blue) and the monoclinic α-WP$_2$ (red). The inset sketches intraband and interband scattering processes. (b) and (c) The crystal structure of both phases with strands of polyhedra forming along the crystallographic a axis and the b axis, respectively.

pronounced T dependence. We propose the highly anisotropic Fermi surfaces have an important role and that intraband and interband fluctuations evolve differently. Microscopic modeling of RS supports these findings. Furthermore, phonons show decisive anomalies in frequency and linewidth with generally larger effects in the topologically trivial α phase. This demonstrates a remarkable interplay and competition of electron-phonon and electron-electron interactions in these phases.

II. EXPERIMENTAL DETAILS

Single crystals of both phases of WP$_2$ were grown via chemical vapor transport [13]. The resulting crystal structure (α or β phase) of the samples depends on a detailed temperature control during the growth process. Orthorhombic β-WP$_2$ crystallizes in space group $Cmc21$, with one W and two P ions located on $4a$ Wyckoff positions and chains of tungsten polyhedra running along the crystallographic a axis. Monoclinic α-WP$_2$ crystallizes in space group $C12/m1$, with one W and two P ions each located on $4i$ Wyckoff positions and chains of tungsten polyhedra running along the crystallographic b axis [10]. The reduced coordination of the latter structural element is also the basis of the quasi-one-dimensional (quasi-1D) character of the electronic states in both phases. Details of the observed phonon modes of both phases can be found in the Appendix. Our room-temperature data are in excellent agreement with a previous study of phonons in β-WP$_2$ [15].

Temperature-dependent RS experiments probing excitations down to 100 cm^{-1} were performed using a Horiba LabRam HR800 spectrometer equipped with a holographic notch filter and an excitation wavelength $\lambda = 532$ nm. Further experiments with a lower cutoff energy of about 30 cm^{-1} were carried out using a Dilor-XY triple spectrometer with an excitation wavelength of 488 nm.

III. RESULTS

A. Phonon scattering

In Fig. 1(a) we compare Raman spectra of α- and β-WP$_2$. Despite similarities, both phases have their very own distribution of phonon frequencies. This also highlights the phase purity of both crystals. We observe 7 out of 9 expected modes from α-WP$_2$ and 13 out of 15 modes from β-WP$_2$. The missing modes are not detected because of their too small intensity or overlap with the observed ones. Note that the intensity of phonon scattering of the two phases is rather similar. This is consistent with a similar electronic polarizability on the energy scale of the incident photons, i.e., approximately 2 eV, irrespective of the existence of low-energy, chiral fermions and broken inversion symmetry. Throughout the paper the data are not scaled to allow a better comparison of the two phases.

We notice a generally larger phonon linewidth in α-WP$_2$ compared to β-WP$_2$. The mean linewidths are $\Delta\omega_{mean} = 3.4$ and 2.6 cm^{-1}, respectively (see also a list of low-temperature data in Tables I and II in the Appendix). It is tempting to attribute the larger linewidth to an enhanced electron-phonon interaction and respective scattering processes that limit the phonon lifetime in α-WP$_2$. More details will be discussed further below.

In Figs. 1(b) and 1(c) sketches of the crystal structure of both phases are given. The ions are coordinated in chains of polyhedra. The chains run along the crystallographic a axis or along the b axis for orthorhombic β- and monoclinic α-WP$_2$, respectively. This structural element is also the basis of the quasi-1D character of the electronic states of both phases.

The temperature-dependent Raman data plotted in Figs. 2(a) and 2(b) show a smooth and gradual evolution of the phonons, without any evidence of a structural phase transition. Therefore, α-WP$_2$ retains its center of inversion, while β-WP$_2$ remains without. For a more detailed analysis, we
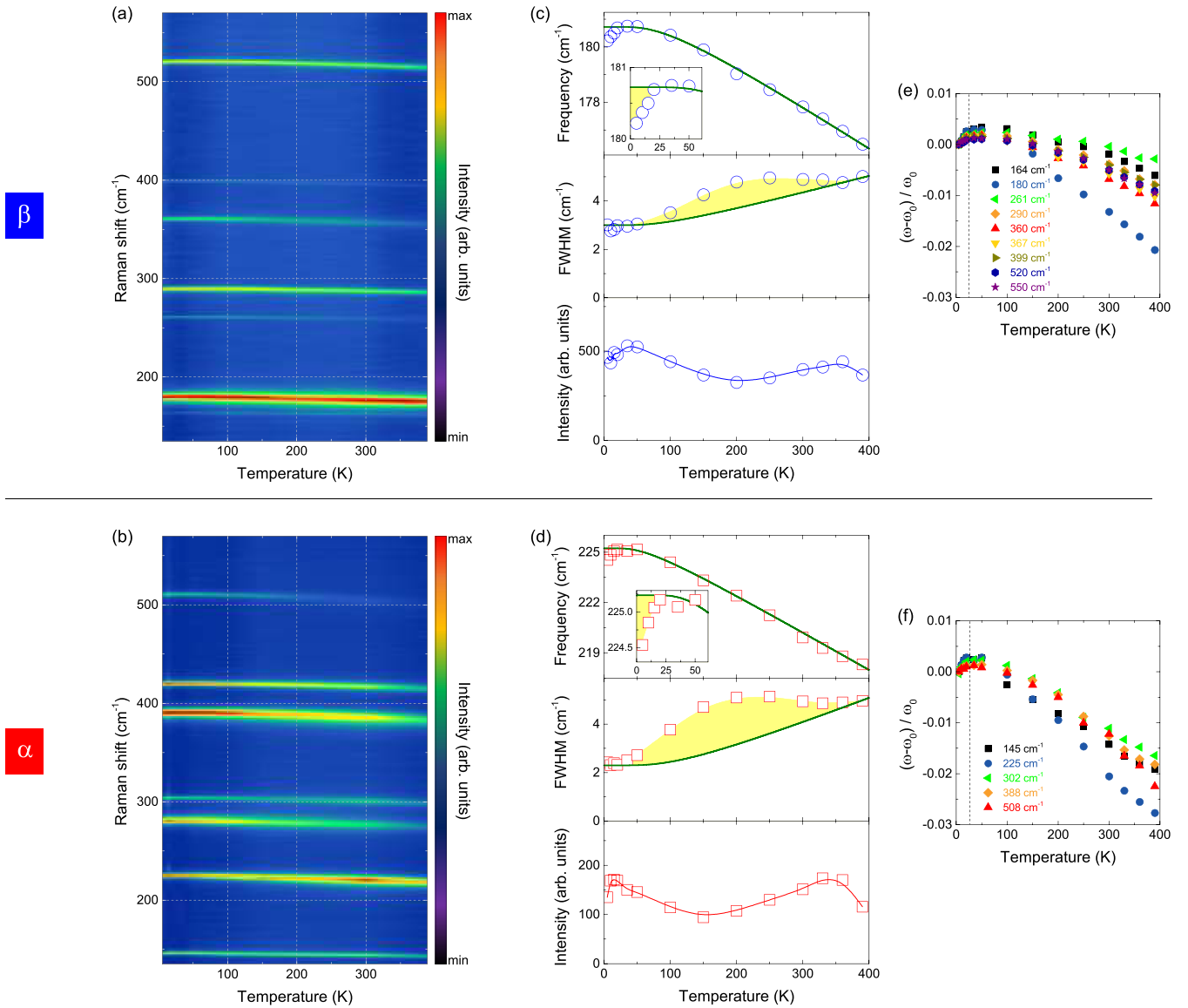
FIG. 2. (a) and (b) Temperature-dependent Raman spectra from the topological β-WP$_2$ and the topologically trivial α-WP$_2$, respectively, as false-color plots. (c) and (d) Detailed analysis of the phonon parameters of the 180-cm^{-1} mode in the β phase and the 225-cm^{-1} mode in the α phase, respectively. (e) and (f) Normalized temperature dependence of phonon frequencies in β- and α-WP$_2$, respectively.

plot the parameters frequency, linewidth, and intensity of one selected phonon mode in Figs. 2(c) and 2(d). Both frequency ω and linewidth Γ can be approximated by first-order anharmonicity [16], with $\omega(T) = \omega_0 - A(1 + \frac{2}{\exp(\hbar\omega_0/2k_BT)-1})$ and $\Gamma(T) = \Gamma_0(\frac{1+B}{\exp(\hbar\omega_0/k_BT)-1})$, where A and B are fitting parameters. This modeling corresponds to a decay of optical phonons into several acoustic phonons with pairwise compensating, large momenta.

While these functions result in an overall reasonable description of the data, there are two temperature regimes with deviations. At low temperatures, $T \lesssim 20$ K, the phonon frequencies show an anomalous softening of both phases; see the insets in Figs. 2(c) and 2(d) for a zoom into the data. It could be tempting to assign this effect to the crossover to hydrodynamic charge transport in β-WP$_2$ [12]. However, for α-WP$_2$ with a similar softening a hydrodynamic transport regime has not been reported. Therefore, a unified approach

must be considered. As both phases are low-dimensional semimetals, enhanced electron-phonon coupling due to intra-band fluctuations [14] of the nested, low-dimensional Fermi surface is more plausible, as we will discuss below.

The second anomalous regime is given at intermediate temperatures, 50 K $< T <$ 300 K. Here, the phonon linewidth shows an anomalous broadening [see the yellow-shaded area in Figs. 2(c) and 2(d)], and the phonon intensities deviate from the expected monotonous behavior. The latter intensities refer to the peak intensities of the phonons. The given picture remains essentially the same if integrated intensities are considered. In this regime of finite temperatures the anomalies may be attributed to a modification of anharmonicity, i.e., optical phonon decay processes into acoustic, zone boundary phonons. This includes all finite-momentum self-energy effects that are relevant for the matrix elements of electron-phonon interaction. It is remarkable that the phonon

TABLE I. Optical phonon modes of the topological, orthorhombic β-WP$_2$ in au polarization. The observed linewidths in FWHM are determined in the low-temperature limit and lead to a mean linewidth of $\Delta\omega_{\mathrm{mean}} = 2.6$ cm^{-1}.

ω_{exp} (cm^{-1})	Assignment	Line shape	Linewidth (cm^{-1})
164	A_2	Lorentz	1.9
174	B_2	Lorentz	3.5
180	A_1	Lorentz	3.0
261	B_1/A_2	Lorentz	1.9
290	A_1	Lorentz	2.4
297	B_2/A_2	Lorentz	2.0
325	B_1	Lorentz	2.4
360	A_1	Lorentz	2.7
367	B_2	Lorentz	2.5
399	A_1	Lorentz	2.2
440	B_2	Lorentz	3.8
520	A_1	Lorentz	2.2
550	B_2	Lorentz	3.0

anomalies quantified by the maximum deviation from the anharmonic fit to the linewidth are larger in the topologically trivial α-WP$_2$.

In Figs. 2(e) and 2(f) the normalized phonon frequencies for most phonon modes are plotted. The low-temperature phonon softening occurs with a comparable magnitude for all modes. The total phonon anharmonicity given by the difference of the frequencies in the low- and high-temperature limits of the phonon frequency data differs from mode to mode and shows a larger magnitude for the higher-frequency phonons. At this point we emphasize that recent photoemission experiments on β-WP$_2$ did not detect a temperature dependence of the Weyl points or other electronic features for energies close to E_F [11]. Therefore, we assume that the electronic structure does not exhibit a general tendency for an instability.

B. Finite energy and quasielastic ERS

Figures 3(a) and 3(b) follow the temperature dependence of the intensity $I(T)$ of a broad continuum that is observed in the frequency range of approximately 100 to 450 cm^{-1} in both phases. The inset shows a zoom into the data of the β phase as an example. This finite-energy continuum points to

TABLE II. Optical phonon modes of the topologically trivial, monoclinic α-WP$_2$ in bu polarization. The observed linewidths in FWHM are determined in the low-temperature limit and lead to a mean linewidth of $\Delta\omega_{\mathrm{mean}} = 3.4$ cm^{-1}. The observed linewidth in the low-temperature limit is given as FWHM.

ω_{exp} (cm^{-1})	Assignment	Line shape	Linewidth (cm^{-1})
145	A_g/B_g	Fano	2.0
225	A_g	Fano	2.4
279	A_g/B_g	Lorentz	4.3
302	B_g	Fano	3.8
388	A_g	Lorentz	4.0
418	A_g	Lorentz	2.5
508	A_g	Lorentz	4.5

multiparticle processes, most likely electronic interband scattering in the semimetal energy landscape. Phonon scattering is not taken into account as there is no evidence of a lifting of momentum conservation that could induce a continuum.

At room temperature these continua have a similar intensity in both phases, and also their polarization vectors are both aligned parallel to the chain of WP coordinations, i.e., along the a axis in the β phase and along the b axis in the α phase. In the β phase and for temperatures below 35 K, $I(T)$ is constant and small. For higher temperatures it is much larger and develops a kind of plateau. This evolution is very close to the temperature dependence of the Lorenz number $L(T)$ of β-WP$_2$ derived from thermal and electrical transport [12] (see the solid green squares). In the α phase $I(T)$ shows a continuous temperature dependence and can be fitted to a power law. Here, no detailed thermal transport data exist so far for a comparison.

In addition, we observe quasielastic scattering (QES; $E \approx 0$) in both phases. In Fig. 3(c) we show Bose-corrected, low-energy data from the β phase and a fit to as-measured data. In Fig. 3(d) we compare the temperature dependence of the dynamic Raman susceptibility, an intensity-related quantity, of both phases. The intensity of QES is larger than that of the finite-energy continuum. It has the same selection rules as the continuum. However, for the α phase QES is also observable with polarizations perpendicular to the chain direction. The inset in Fig. 3(d) gives the Bose-corrected intensity $I_{\mathrm{QES}}/(n+1)$ of QES with the Bose factor $n(\omega, T)$. For β-WP$_2$ we find a pronounced and asymmetric peak from 10 to 50 K in the evolution of $I_{\mathrm{QES}}/(n+1)$ with temperature and a maximum at $T_{\mathrm{max}} = 15$ K. At the lowest temperatures the intensity collapses to a minimum comparable to the room-temperature value. At high temperatures there exists a linear decrease with temperature. For α-WP$_2$ $I_{\mathrm{QES}}/(n+1)$ is less pronounced with a shallower maximum and a flatter high-temperature tail.

ERS in simple metals is related to electronic density fluctuations due to intraband excitations and is difficult to observe due to its small intensity because of screening [17,18]. In bad metals it is easier to observe due to its finite-energy maximum with a peak related to the scattering rate. Finally, in the limit of a marginal Fermi liquid with diffusive dynamics [19] ERS can be observed over an extended continuum of energy. We refer here to high-temperature superconductors based on cuprates [20] and ferropnictides [21]. For the latter nesting is also an important ingredient. QES and low-energy maxima are also observed in topological insulators [22,23], the Dirac semimetal Cd$_3$As$_2$ [8], and single and bilayer graphene [24–26]. The intensity $I(T)$ of ERS in Cd$_3$As$_2$ is similar to the data shown in Fig. 3. For a microscopic approach to this scattering in topological semimetals we refer to the Appendix detailing the evaluation of scattering Hamiltonians.

For an analysis of ERS the following treatment has been developed: A Bose correction with $I(\omega) = [1 + n(\omega, T)]\chi''(\omega)$ leads to the Raman susceptibility $\chi''(\omega)$ and the Raman conductivity $\chi''(\omega)/\omega$. In an ansatz analogous to the Kramers-Kronig relation a dynamic Raman susceptibility is defined, $\chi^{\mathrm{dyn}} = \lim_{\omega \to 0} \chi(k = 0, \omega) \equiv \frac{2}{\pi}\int_0^\infty \frac{\chi''(\omega)}{\omega}d\omega$ [27]. The latter quantity successfully describes dynamic electronic properties, e.g., inter- and intraband fluctuations in
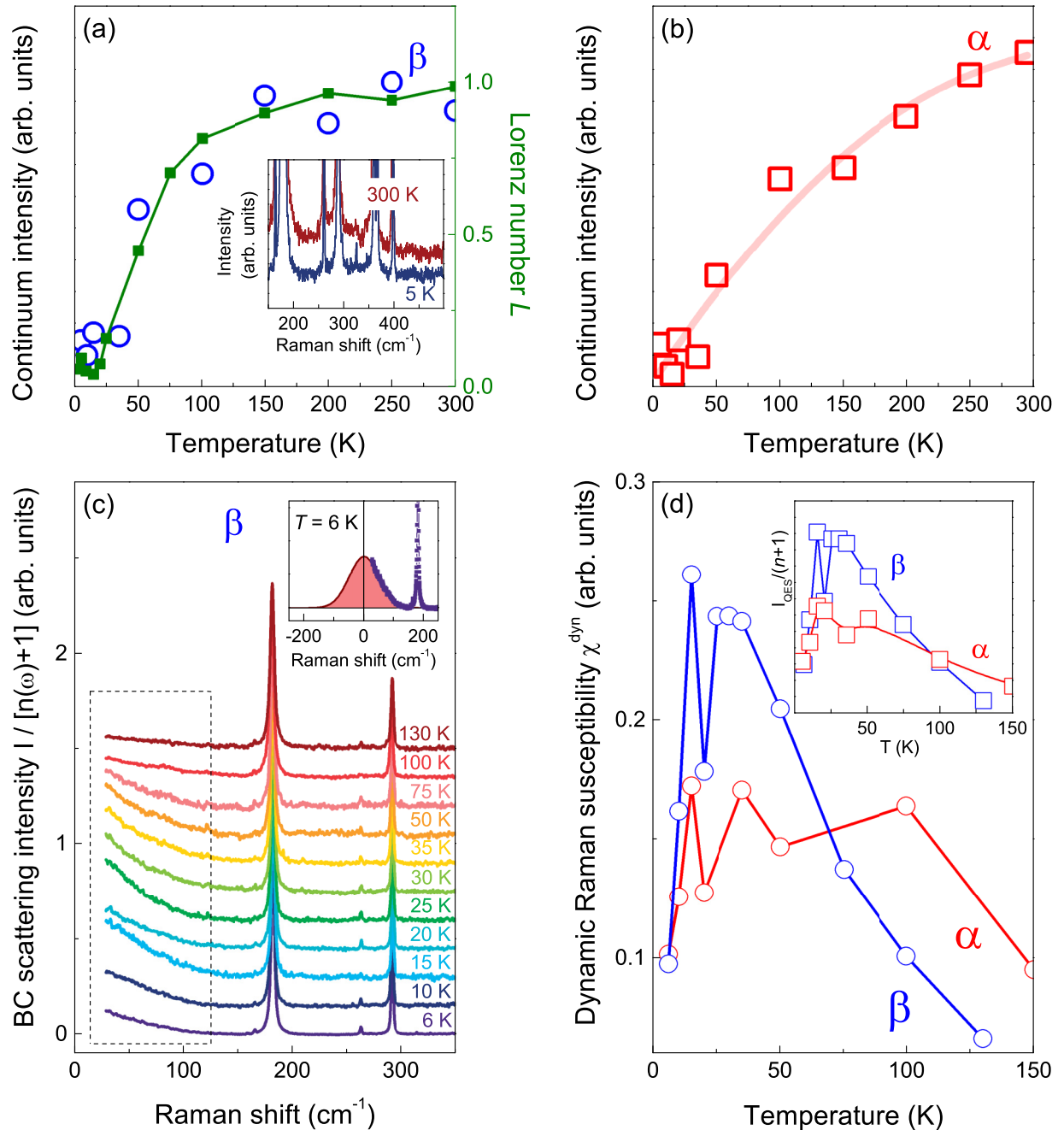
FIG. 3. (a) Intensity $I(T)$ of a finite-energy continuum of β-WP$_2$, shown as blue circles. The Lorenz number $L(T)$ from thermal and electrical transport in β-WP$_2$ [12] is also shown (green squares). The inset gives as-measured Raman spectra of β-WP$_2$ at 300 K (red) and 5 K (blue). (b) Intensity $I(T)$ of the continuum of α-WP$_2$ (red squares) together with a power law fit (red line). (c) Bose-corrected Raman spectra of the low-energy regime of β-WP$_2$ with quasielastic scattering. The inset shows a fit of the as-measured, 6 K Raman data to a Lorentzian. (d) Dynamic Raman susceptibility as a function of temperature derived from a frequency integration of I_{QES} from 150 to 500 cm^{-1}. The inset shows the Bose-corrected intensity $I_{QES}/(n+1)$ of both phases.

Fe-based superconductors that are complex due to the multisheet Fermi surface and pronounced nesting [27].

For the β phase $\chi^{dyn}(T)$ shows a broad, asymmetric maximum at $T_{max} = 25$ K with a sharp drop at low temperatures [see Fig. 3(d), blue curve]. For the α phase the maximum is less obvious and shifted to higher temperatures (red curve). This quantity was obtained from an integration 150 to 500 cm^{-1}. We find the enhanced χ^{dyn} of the β phase with respect

to the α phase most significant as it has to be related to enhanced electronic fluctuations. This effect is also obvious in the Bose-corrected data. In addition to this data analysis we checked for characteristic effects based on energy density fluctuations, e.g., due to some order suppressed by low dimensionality [28] and to scaling of the data known from precursors of a phase transition [29]. The available data do not support such approaches. Therefore, we do not discuss them here anymore.

IV. DISCUSSION

The semimetal WP_2 with the two phases α-WP_2 and β-WP_2 offers the unique opportunity to evaluate the effects of topological invariants on electronic fluctuations and phonons. The most prominent shared properties are given by deviations of the optical phonons from conventional anharmonicity, i.e., the low-temperature softening and the intermediate-temperature broadening in the interval 50–350 K. These anomalies are also evident in the phonon intensity, and they are not restricted to a particular mode. This means that they do not evidence a lattice instability of a particular form. Instead, for both phases they reflect the consequence of low dimensionality given by the chain of tungsten ions and the very anisotropic Fermi surfaces with evidence for nesting [12,14]. A conventional structural instability, however, is prohibited by the low site symmetry, which does not support releasing degeneracies. This is consistent with the absence of temperature-dependent features of the Fermi surface [11].

Subtler differences exist in an enhanced magnitude of these effects for the α phase. This means that the topologically trivial phase has a larger electron-phonon coupling and, accordingly, that this coupling is not essential for transport anomalies of the topological phase. This conclusion is diametrical to a theoretical consideration of phonon scattering processes in β-WP_2 [15]. On the other hand, the observed anomalies do not contradict the present knowledge of topologically induced phonon anomalies [4–7]. A general approach for semimetals shows that the respective matrix elements have a strong momentum dependence and differentiate inter- vs intraband transitions [see the inset in Fig. 1(a)]. Intraband fluctuations with small k are related to weaker phonon anomalies, while interband fluctuations couple rather efficiently to phonons at large k. We attribute the observed finite-temperature effects in WP_2 to deviations from conventional anharmonicity involving phonon decay processes. These processes involve phonons with large momenta up to the zone boundary. The Bose factor $n(\omega, T)$ that describes their thermal occupation leads to a low-temperature onset of additional linewidth for $T \gtrsim 50$ K. The high-frequency cutoff of the acoustic phonon branches at the zone boundary is compatible with the upper temperature limit of the anomalies. Together, this leads to a finite-temperature interval of enhanced linewidth. Such well-defined intervals of phonon anomalies [30] together with the corresponding ERS [25,26] have already been observed in electrically tuned bilayer graphene.

In the following we will discuss ERS as the second shared property of the WP_2 phases. We tentatively attribute the finite-energy continuum to interband scattering and the QES to intraband scattering. This is based on their different typical energy scales. The similarity of $I(T)$ of QES in the β phase to its Lorenz number $L(T)$ therefore results from intraband fluctuations being a dominant scattering process at low temperatures (in the hydrodynamic transport regime). Its evolution consists of a gradual narrowing of the quasiparticle peak with decreasing temperatures leading to a reduced spectral weight in the energy window of the Raman scattering experiments.

It is interesting to note that the topological β phase shows a more pronounced dependence $I(T)$ than the α phase, despite larger phonon anomalies in the latter. On the other hand, one would expect a more pronounced temperature dependence as the low-temperature regime is characterized by hydrodynamic charge transport. At this point we refer to the drastic enhancement and following collapse of χ^{dyn} preceding the onset of coherent charge transport towards low temperatures. The underlying finite-energy RS continuum is a rather rare observation for a metal and is attributed to diffusive dynamics or marginal quasiparticles. The latter are attributed to low-dimensionality and nesting of the Fermi surface. The drop in $I(T)$ of the finite-energy continuum corresponds to a crossover from a marginal Fermi liquid to a coherent regime that has frequently been discussed in strongly correlated systems [19]. The observed hydrodynamic transport is a result of the coherence probed by interband fluctuations in RS.

The implications of low-dimensionality and nesting of the Fermi surface are furthermore highlighted by the selection rules of the electronic Raman scattering. Its intensity is observed with incident and scattered photons polarized parallel to the chain direction. In contrast, a microscopic evaluation of scattering rates and intensities based on Green's functions for isotropic electronic bands leads to the dominance of crossed polarizations (see the Appendix). Therefore, low dimensionality plays an important role for both phases of WP_2, presently defying microscopic modeling.

V. SUMMARY

Summarizing, we probed a dichotomy of interband and intraband scattering processes in WP_2 on different energy scales. The temperature dependences of the respective RS intensities show an abrupt collapse with strongly reduced scattering rates that heralds the more coherent regime of hydrodynamic transport. This collapse is observed only in the topological phase of WP_2. The pronounced T dependence of quasielastic scattering can be mapped on the Lorenz number $L(T)$ derived earlier from transport experiments. Electron-phonon coupling is significant for both phases due to nesting. However, this coupling is stronger in the topologically trivial phase of WP_2.

APPENDIX

1. Phonon analysis

For orthorhombic β-WP_2 in $Cmc2_1$ with one W and two P ions located on $4a$ Wyckoff positions a factor-group analysis leads to $5A_1 + 3A_2 + 2B_1 + 5B_2 = 15$ Raman-active optical
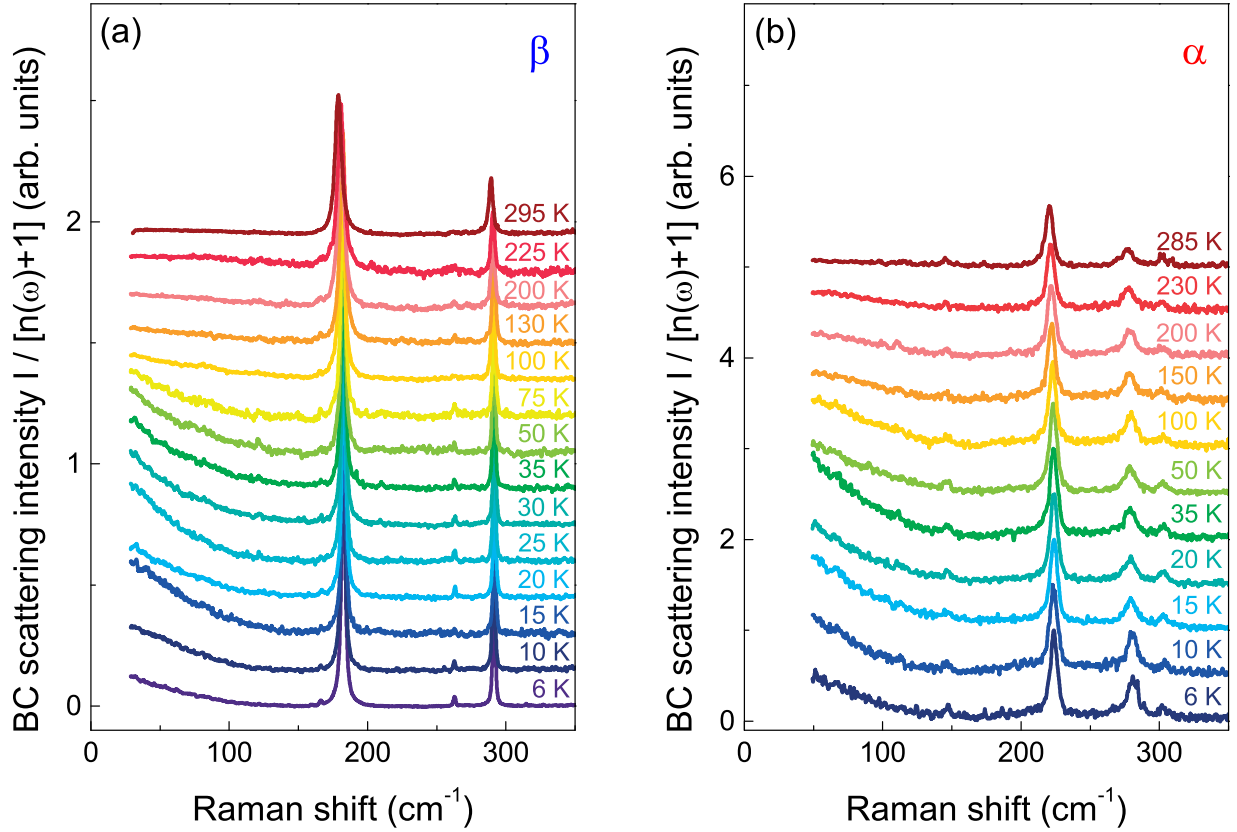
FIG. 4. (a) Bose-corrected Raman spectra of the low-energy regime of β-WP$_2$ for different temperatures. (b) Bose-corrected Raman spectra of the low-energy regime of α-WP$_2$ for different temperatures.

phonon modes. The experimentally determined phonon frequencies and linewidths are detailed in Table I.

Monoclinic α-WP$_2$ in $C12/m1$ with one W and two P ions each located on $4i$ Wyckoff positions [10] yields $6A_g + 3B_g = 9$ Raman-active optical phonon modes. Details on the phonon assignment, energies, and linewidths can be found in Table II.

2. Quasielastic scattering: A comparison

To allow a better comparison, Fig. 4 shows side by side Bose-corrected Raman scattering spectra of the topological β-WP$_2$ and the topologically trivial α-WP$_2$. The different temperature evolutions of the low-energy response are also evident from the data given in Figs. 3(a) and 3(b).

3. ERS in topological semimetals

ERS was established early on as a valuable tool to probe inter- and intraband scattering, screening, and electronic correlations [17,18,20]. Here, we establish a formal-

ism needed to understand fluctuation effects and ERS in semimetals with chiral, low-energy fermions using scattering rates derived from the chiral Green's function [31]. Based on transport experiments and theoretical considerations hydrodynamic charge dynamics exist in the topological phase of WP$_2$. Therefore, we consider particle and hole contributions to account for elastic scattering of intraband electrons in the Weyl semimetal.

a. Scattering rates $1/\tau$

In Weyl semimetals the particle and hole contributions for small q are given by the chiral Green's functions $G_L(\vec{k}, iv_n)$ (for the left chirality) and $G_R(\vec{k}, iv_n)$ (for the right chirality):

$$G_L(\vec{k} + \vec{q}, iv_n) = \frac{1}{iv_n + \mu - \epsilon(\vec{k} + \vec{q})} + \frac{1}{iv_n + \mu + \epsilon(\vec{k} + \vec{q})}$$

$$\approx \frac{1}{iv_n - \epsilon(\vec{k}) + \mu} + \frac{1}{iv_n + \epsilon(\vec{k}) + \mu}.$$

The dispersion for the left chirality $\epsilon(\vec{k}) = \sqrt{v^2[k^2 + (k_3 - Q_3)^2]}$. Q_3 is the momentum of the node in the z direction. In the experiment several nodes exist:

$$\sum(\vec{k}, iv_n) = -\frac{1}{\beta} \int \frac{d^3q}{(2\pi)^3} \sum_n [G_L(\vec{k} + \vec{q}, iv_n)]D(\Omega_q, iv_n - i\omega_n)$$

$$\approx \int \frac{d^3q}{(2\pi)^3} \frac{1}{2\pi i} \int_c G_L(\vec{k}, z)D(\Omega_q, iv_n - z)f(z)dz$$

$$= \int \frac{d^3q}{(2\pi)^3} \frac{1}{2\pi i} \int_c f(z) \left(\frac{1}{z - \epsilon(\vec{k}) + \mu} + \frac{1}{z + \epsilon(\vec{k}) + \mu} \right) \frac{2\Omega(q)}{(-i\nu_n - i\omega_n)^2 - \Omega(q)^2},$$

$$f(z) = \frac{1}{e^{\beta z} + 1}, \quad D(\Omega_q, i\nu_n - i\omega_n) = \frac{2\Omega_q}{(i\nu_n - i\omega_n)^2 - \Omega_q^2}. \tag{A1}$$

Here, ω_n is the Matsubara frequency $2\pi T(n + 1/2)$, and Ω_q is the phonon frequency which corresponds to momenta q. We compute the contribution from the poles, perform the analytic continuation, and find, for the frequency ω at finite temperature,

$$\frac{1}{\tau} = \int \frac{d^3q}{(2\pi)^3} \left[\left\{ f[-\epsilon(\vec{k}) + \mu] \frac{2\Omega_q}{[\omega - \epsilon(\vec{k}) + \mu]^2 - \Omega_q^2 + i\eta} \right\} + \left\{ f[-\epsilon(\vec{k}) - \mu] \frac{2\Omega_q}{[\omega - \epsilon(\vec{k}) + \mu]^2 - \Omega_q^2 + i\eta} \right\} \right.$$

$$+ \left(\frac{1}{1 - e^{\beta\Omega_q}} \right) \left(\frac{1}{\omega - \epsilon(\vec{k}) + \mu + \Omega_q + i\eta} + \frac{1}{\omega - \epsilon(\vec{k}) + \mu + \Omega_q + i\eta} \right)$$

$$\left. \times \left(\frac{1}{1 - e^{-\beta\Omega_q}} \right) \left(\frac{1}{\omega - \epsilon(\vec{k}) + \mu - \Omega_q + i\eta} + \frac{1}{\omega + \epsilon(\vec{k}) + \mu - \Omega_q + i\eta} \right) \right]. \tag{A2}$$

Ignoring the *Fermi-Dirac* contribution, we obtain at low temperature

$$\frac{1}{\tau} = \text{Im} \sum (\vec{k}, \omega) = \frac{g_{e_{ph}}^2}{2(2\pi)^2} \int d^3q \left[\left(\frac{1}{1 - e^{\beta\Omega_q}} \right) \delta[\omega - \epsilon(\vec{k}) + \mu + \Omega_q] - \left(\frac{1}{1 - e^{\beta\Omega_q}} + 1 \right) \delta(\omega - \epsilon(\vec{k}) + \mu - \Omega_q) \right]. \tag{A3}$$

Here, $g_{e_{ph}}^2$ is the electron-phonon coupling parameter. For acoustic phonons, $\Omega_q \approx C|q|$, the scattering rate is

$$\frac{1}{\tau} = \frac{g_{e_{ph}}^2}{C^3 2(2\pi)^2} \left\{ [\omega - \epsilon(\vec{k}) + \mu]^2 \left(\frac{1}{1 - e^{\hbar v \beta(\omega - \epsilon(\vec{k}) + \mu)}} \right) - [\omega - \epsilon(\vec{k}) + \mu]^2 \left(\frac{1}{1 - e^{\hbar v \beta[-\omega + \epsilon(\vec{k}) - \mu]}} \right) \right\} \propto T.$$

For optical phonons, $\Omega_q = \Omega_0 - \alpha q^2$, the scattering rate is

$$\frac{1}{\tau} = \frac{g_{e_{ph}}^2}{45(2\pi)^2} \left[\sqrt{[-\omega + \epsilon(\vec{k}) - \mu + \Omega_0]} \left(\frac{1}{1 - e^{\hbar v \beta(-\omega + \epsilon(\vec{k}) - \mu)}} \right) - \sqrt{[\omega - \epsilon(\vec{k}) + \mu - \Omega_0]} \left(\frac{1}{1 - e^{\hbar v \beta[\omega - \epsilon(\vec{k}) + \mu]}} \right) \right]. \tag{A4}$$

b. Raman Scattering in the topological phase

The excited bands have left (L) and right (R) chirality. Phonons couple to intraband excitations, and we have an $L^\dagger L$ phonon, and $R^\dagger R$ phonon, and H.c. Light couples the ground state (the valence band) to the excited left or right chiral bands (ground state). This leads to the $V^\dagger L$ photon, $V^\dagger R$ photon, and H.c. The resulting triangle diagrams have important implications for the selection rules of light scattering, i.e., an effect of the polarization of light in the Raman scattering experiment. We notice that significant scattering will occur when $\vec{E}_{\text{in}}$ is perpendicular to $\vec{E}_{\text{out}}$. In such a case we have the unique chance to probe the winding number $J = 1, 2$ introduced by Carbotte [32] for a topological semimetal using Raman scattering. The experimental data, however, show a dominance of electronic Raman scattering in polarizations parallel to the chainlike crystallographic coordination. We

attribute this to the strongly anisotropic band structure that has presently not been taken into account.

Nevertheless, the scattering involves separately left and right excited chiral bands, and the valence band ground state is given by the Green's function $g_{valence}$. The Green's functions of the chiral electrons are G_{Left} and G_{Right}:

$$S_L^{(3)} = \int d^3x_1 \int dt_1 \int d^3x_2 \int dt_2 \int d^3x_3 \int dt_3$$

$$\times \text{Tr}[G_{Left}(\vec{x}_2, t_2; \vec{x}_1, t_1)\varphi(\vec{x}_2, t_2)G_{Left}(\vec{x}_3, t_3; \vec{x}_2, t_2)$$

$$\times \sigma_1 \cdot \vec{A}_1(\vec{x}_3, t_3)g_{valence}(\vec{x}_1, t_1; \vec{x}_3, t_3)\sigma_2 \cdot \vec{A}_2(\vec{x}_1, t_1)]. \tag{A5}$$

A similar contribution comes from the other chiral band giving $S_R^{(3)}$. The Raman intensity is then given by $I = |S_L^{(3)} + S_R^{(3)}|^2$. Due to interference effects the latter intensity may decrease with the onset of coherence.

[1] K. Manna, Y. Sun, L. Müchler, J. Kübler, and C. Felser, Nat. Rev. Mater. **3**, 244 (2018).

[2] B. Yan and C. Felser, Annu. Rev. Condens. Matter Phys. **8**, 337 (2017).

[3] W. Witczak-Krempa and Y. B. Kim, Phys. Rev. B **85**, 045124 (2012).

[4] I. Garate, Phys. Rev. Lett. **110**, 046402 (2013).

[5] K. Saha, K. Légaré, and I. Garate, Phys. Rev. Lett. **115**, 176405 (2015).

[6] J. Coulter, G. B. Osterhoudt, C. A. C. Garcia, Y. Wang, V. Plisson, B. Shen, N. Ni, K. S. Burch, and P. Narang, Phys. Rev. B **100**, 220301(R) (2019)

[7] A. Metavitsiadis and W. Brenig, Phys. Rev. B **101**, 035103 (2020).

[8] A. Sharafeev, V. Gnezdilov, R. Sankar, F. C. Chou, and P. Lemmens, Phys. Rev. B **95**, 235148 (2017).

[9] H. Chen, Y. Li, H. Wu, Y. Peng, Y. Fang, C. Chen, S. Xie, and L. Song, Solid State Commun. **289**, 56 (2019).

[10] R. Rühl and W. Jeitschko, Monatsh. Chem. **114**, 817 (1983).

[11] E. Razzoli, B. Zwartsenberg, M. Michiardi, F. Boschini, R. P. Day, I. S. Elfimov, J. D. Denlinger, V. Süss, C. Felser, and A. Damascelli, Phys. Rev. B **97**, 201103(R) (2018).

[12] J. Gooth, F. Menges, N. Kumar, V. Süss, C. Shekhar, Y. Sun, U. Drechsler, R. Zierold, C. Felser, and B. Gotsmann, Nat. Commun. **9**, 4093 (2018).

[13] N. Kumar, Y. Sun, N. Xu, K. Manna, M. Yao, V. Süss, I. Leermakers, O. Young, T. Förster, M. Schmidt, H. Borrmann, B. Yan, U. Zeitler, M. Shi, C. Felser, and C. Shekhar, Nat. Commun. **8**, 1642 (2017).

[14] J. Du, Z. Lou, S. N. Zhang, Y. Zhou, B. Xu, Q. Chen, Y. Tang, S. Chen, H. Chen, Q. Zhu, H. Wang, J. Yang, Q. S. Wu, O. V. Yazyev, and M. Fang, Phys. Rev. B **97**, 245101 (2018).

[15] B. Su, Y. Song, Y. Hou, X. Chen, J. Zhao, Y. Ma, Y. Yang, J. Guo, J. Luo, and Z.-G. Chen, Adv. Mater. **31**, 1903498 (2019).

[16] M. Balkanski, R. F. Wallis, and E. Haro, Phys. Rev. B **28**, 1928 (1983).

[17] E. Burstein, D. L. Mills, and R. F. Wallis, Phys. Rev. B **4**, 2429 (1971).

[18] M. V. Klein, in *Light Scattering in Solids*, edited by M. Cardona (Springer, Berlin, 1983).

[19] Ch. M. Varma, Phys. Rev. B **96**, 075122 (2017).

[20] T. P. Devereaux and R. Hackl, Rev. Mod. Phys. **79**, 175 (2007).

[21] N. Lazarevic and R. Hackl, J. Phys. Condens. Matter **32**, 413001 (2020).

[22] V. Gnezdilov, Yu. G. Pashkevich, H. Berger, E. Pomjakushina, K. Conder, and P. Lemmens, Phys. Rev. B **84**, 195118 (2011).

[23] V. Gnezdilov, P. Lemmens, D. Wulferding, A. Möller, P. Recher, H. Berger, R. Sankar, and F. C. Chou, Phys. Rev. B **89**, 195117 (2014).

[24] Yu. S. Ponosov, A. V. Ushakov, and S. V. Streltsov, Phys. Rev. B **91**, 195435 (2015).

[25] E. Riccardi, M.-A. Measson, M. Cazayous, A. Sacuto, and Y. Gallais, Phys. Rev. Lett. **116**, 066805 (2016).

[26] E. Riccardi, O. Kashuba, M. Cazayous, M.-A. Méasson, A. Sacuto, and Y. Gallais, Phys. Rev. Mater. **3**, 014002 (2019).

[27] Y. Gallais and I. Paul, C. R. Phys. **17**, 113 (2016).

[28] P. Lemmens, G. Güntherodt, and C. Gros, Phys. Rep. **375**, 1 (2003).

[29] A. Glamazda, P. Lemmens, S.-H. Do, Y. S. Choi, and K.-Y. Choi, Nat. Commun. **7**, 12286 (2016).

[30] J. Yan, E. A. Henriksen, Ph. Kim, and A. Pinczuk, Phys. Rev. Lett. **101**, 136804 (2008).

[31] G. D. Mahan, *Many-Particle Physics* (Kluwer/Plenum, New York, 2000).

[32] S. P. Mukherjee and J. P. Carbotte, Phys. Rev. B **97**, 045150 (2018).